

Laser-driven shock-wave propagation in pure and layered targets

David Salzmann, Shalom Eliezer, Aaron D. Krumbein, and Leah Gitter

Soreq Nuclear Research Centre, Yavne 70600, Israel

(Received 3 December 1981; revised manuscript received 21 September 1982)

The propagation properties of laser-driven shock waves in pure and layered polyethylene and aluminum slab targets are studied for a set of laser intensities and pulse widths. The laser-plasma simulations were carried out by means of our one-dimensional Lagrangian hydrodynamic code. It is shown that the various parts of a laser-driven compression wave undergo different thermodynamic trajectories: The shock front portion is on the Hugoniot curve whereas the rear part is closer to an adiabat. It is found that the shock front is accelerated into the cold material till $t \approx 0.8\tau$ (where τ is the laser pulse width) and only later is a constant velocity propagation attained. The scaling laws obtained for the pressure and temperature of the compression wave in pure targets are in good agreement with those published in other works. In layered targets, high compression and pressure were found to occur at the interface of CH₂ on Al targets due to impedance mismatch but were not found when the layers were reversed. The persistence time of the high pressure on the interface in the CH₂ on Al case is long enough relative to the characteristic times of the plasma to have an appreciable influence on the shock-wave propagation into the aluminum layer. This high pressure and compression on the interface can be optimized by adjusting the CH₂ layer thickness.

I. INTRODUCTION

It has been known for many years that laser-plasma interaction can generate a strong shock wave propagating into the cold material. The pressure of these shocks may attain values up to a few terapascals, far beyond the pressures achievable in laboratory experiments and comparable to the pressures measured in nuclear-explosion-driven shock waves. The formation of shock waves in this range has opened up a new regime of the state of matter to laboratory experimentation, in which the equation of state (EOS) of dense and hot material can be studied. Experimental determination of the EOS in this density and pressure region gains special importance because in this domain, unlike much higher or lower densities and pressures, the current theories have predictions of rather low accuracy.¹

The feasibility of the experimental study of EOS by means of laser-induced shock waves was thoroughly studied by Trainor *et al.*¹ and by More.² Experiments were carried out on transparent materials such as solid hydrogen^{3,4} and Plexiglas,⁴ on stepped aluminum⁵⁻⁸ targets and polyethylene slabs.⁹ All these experiments are based on precise measurements of the shock-wave velocities in a slab of pure material, mainly, because these velocities are currently the parameters that can be measured to the highest accuracy.

The measurement of the shock velocity does not

provide sufficient information about the EOS. In fact, the five parameters defining a shock wave (shock velocity v_s , particle velocity U , density ρ , pressure P , and internal energy E) are related by three conservation laws (mass, momentum, and energy), therefore, the measurements of any two of the above parameters is a prerequisite to finding the other three. A second candidate for measurement is the particle velocity measured either by the unloading velocity of a planar target backsurface⁸ (below 0.1 TPa), or by using x-ray backlighting of the target, and measuring the change of the x-ray absorption rate with an ultrafast x-ray streak camera.¹ These experiments have lower accuracy than the shock velocity measurement and they both are at the earliest stage of design and measurement.

Another proposal to find the EOS of a particular material is by an impedance-matching experiment. This technique involves the propagation of a shock from a standard material into an unknown sample. By measuring v_s in both materials and matching the boundary conditions, one can determine the EOS of the unknown relative to that of the standard.^{1,2} This technique is similar to that used in routine impedance-matching experiments,¹⁰ however, the much smaller dimensions of the laser-driven shock-wave targets and the shorter time scale of the physical phenomena pose special problems which are worth thorough study. In fact, a shock-wave incident on the interface between two layers is partial-

ly backreflected and partially transmitted, the percentage of these two waves depending on the shock impedance,¹¹ ρv_s (ρ , density; v_s , shock speed), of the two materials. When the impedances do not completely match, high compressions develop on the interface. Two aspects of this behavior are discussed in this paper. These are (a) that the compression on the interface is optimizable by properly choosing the thickness of the material facing the laser beam and (b) that the shock front is accelerated into the rear material.

The common point to all the above proposals and experiments is the measurement of the shock velocity either in pure material or in layered targets. It seems, therefore, that a detailed analysis of the shock velocity in these targets is highly desirable.

The aim of this paper is to study the propagation of shock waves in pure and layered targets of aluminum and polyethylene with special emphasis on the behavior of the shock velocity and its relation to other shock parameters. We particularly considered the propagation of the shock across the interface between two different material media. Some preliminary calculations have already been reported.¹²

For the sake of illustration, we concentrated on targets of CH_2 and aluminum as these are materials used in previous experiments.^{5-7,9} Our selection of materials was also influenced by our previous experience with such composite targets¹³ and the availability of a complete set of atomic data for them.¹⁴ The 1.06- μm wavelength laser in an intensity range of 3×10^{13} – 3×10^{14} W/cm^2 and a modified Gaussian pulse shape with widths of 300, 600, and 1000 psec were chosen, to make the calculations close to the experimental range recently proposed in the literature.^{1,2}

II. COMPUTER CODE

The computer program used in the calculations is a one-dimensional Lagrangian hydrodynamic laser-plasma simulation code which is based, in part, on the SUPER code.¹⁵ It contains the following features:

(1) one dimensional, two temperature Lagrangian hydrodynamics;

(2) inverse bremsstrahlung absorption of the laser energy up to the critical layer. A modified Gaussian pulse shape was used for the laser pulse, with a linear ramp during the pulse rise and a Gaussian variation during the decay. All the laser energy not absorbed up to the critical layer was assumed to be absorbed at the critical surface itself;

(3) classical heat conduction to transfer energy from the critical to the ablation surface;

(4) non-LTE atomic physics is incorporated to calculate the average degree of ionization, the ioni-

zation energy, and the various radiation rates (free-free, free-bound, and bound-bound);

(5) the code includes a three-step approach to the pressure: (a) zero pressure below vaporization temperature, (b) perfect gas law between vaporization and the temperature of the first ionization energy, (c) Fermi-Dirac degenerate electron gas pressure above the first ionization temperature.¹⁶ A smoothing procedure is used near the boundaries between the three domains;

(6) a perfect degenerate Fermi-Dirac electron gas EOS is incorporated.¹⁶

(7) The code is able to calculate the behavior of layers of different materials, which may have different values of Z . The boundary conditions between two different layers is the requirement of pressure equalization on the interface.

A variable cell size was used with the thinner cells on the side struck by the laser beam. The outermost cell thickness was in the vicinity of 0.05–0.1 μm with a gradual increase of 4–5% per cell to the innermost one. There was no significant change in the results of the computation with a finer mesh (~ 100 Å).

The computer code lacks the ability to deal with three phenomena, namely, resonant and parametric instability absorption, heat transport inhibition, and suprathermal electrons. At a laser intensity of 3×10^{14} W/cm^2 the influence of these three processes is already measurable, but probably is still marginal. The exclusion of these processes from the calculation seems to have some quantitative effect on our results, but as the main point of the present

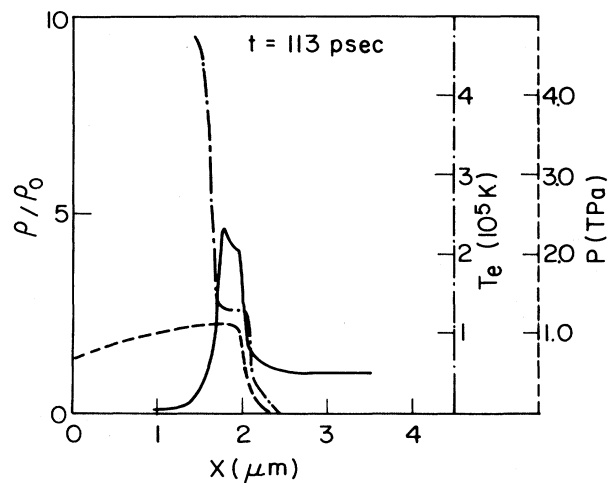
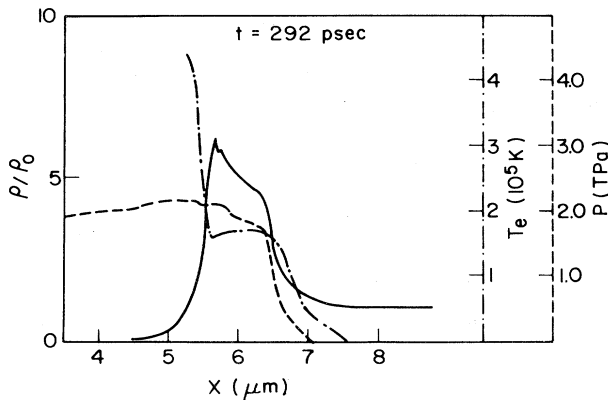


FIG. 1. Spatial profiles of pressure (---), compression (—), and temperature (— · —) in the compression wave driven in a planar aluminum slab irradiated by an $I = 3 \times 10^{14}$ W/cm^2 , $\tau = 600$ -psec laser beam, at $t = 113$ psec after the beginning of the laser pulse.

FIG. 2. Same as Fig. 1 at $t = 292$ psec.

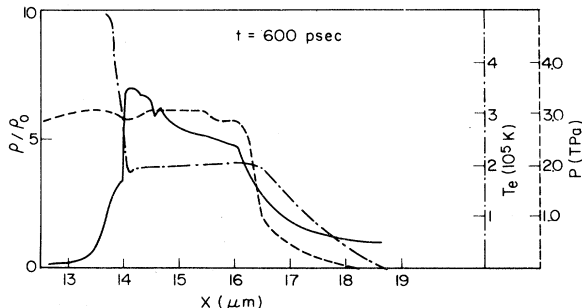
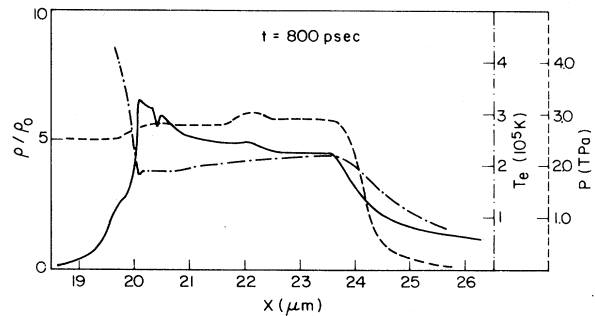
work depends on the hydrodynamics of the problem, qualitatively our calculations are certainly correct. Moreover, comparison of our results with computations which include these phenomena (see Sec. III) reveals that even the quantitative differences are rather small.

III. PROPERTIES OF LASER-DRIVEN SHOCK WAVES

The laser energy absorbed near the critical surface is transported into the solid target by electronic heat conduction. The heated material is blown off the target, and this ablation drives a shock wave into the solid material ahead of the ablating surface.

The pressure exerted by the ablation surface generates a series of weak shock waves, eventually converging into a compression wave. The time evolution of this compression wave is illustrated in Figs. 1–4 for an aluminum slab irradiated with a 3×10^{14} -W/cm², 600-psec laser pulse. At early times, there is a pile up of the weak shock waves into a compression wave, which can be regarded as a multiple-shock wave (see Fig. 1). During this period the compression wave is accelerated into the solid target.

As the pressure increases, the multiple-shock wave coalesces into a single shock as expected from

FIG. 3. Same as Fig. 1 at $t = 600$ psec.FIG. 4. Same as Fig. 1 at $t = 800$ psec.

basic principles.¹¹ However, as long as the laser irradiation continues, shock waves keep on arriving at the rear portion of the compression wave, producing two separate regions which have no sharp boundary between them as in the following: (i) a multiple shock, or “pile-up” zone, in the rear portion of the wave where the incoming shocks from the ablation surface pile up, and (ii) a shock front zone in the frontal part of the wave propagating into the solid material ahead of the pile-up zone (see Figs. 2 and 3).

The propagation velocities of both regions are not constant and the velocity of the pile-up zone being that of a multiple-shock wave, it is generally lower than the velocity of the shock front portion.¹¹ The pile-up zone of the wave can be identified with a higher compression than predicted from a single-shock Hugoniot relation. The difference in the velocities between the regions of the wave causes the broadening of the compression wave as it propagates deeper into the solid material (see Fig. 4). Upon the decrease of the laser pulse, the pressure at the ablation surface drops and a rarefaction wave propagates into the target, eventually overtaking and attenuating the shock. First, the pile-up zone disappears and finally the frontal portion as well. As a result a single shock in the pile-up zone never materializes.

A simple and useful relation was derived by Kidder¹⁷ between the pressure P and the laser intensity I assuming a pure shock-wave propagation

$$P = 1.18 \left[\frac{A}{Z} \right]^{1/3} \left[\frac{I}{10^{14} \text{ W/cm}^2} \right]^{2/3} \text{ TPa} . \quad (3.1)$$

Here A is the atomic weight and Z the average degree of ionization. Equation (3.1) predicts that the pressure is almost independent of the target material. More accurate estimates at a depth of 25 μm in an aluminum target were derived from detailed computer simulations²

$$P = 0.86 \left[\frac{I}{10^{14} \text{ W/cm}^2} \right]^{0.82} \text{ TPa} . \quad (3.2)$$

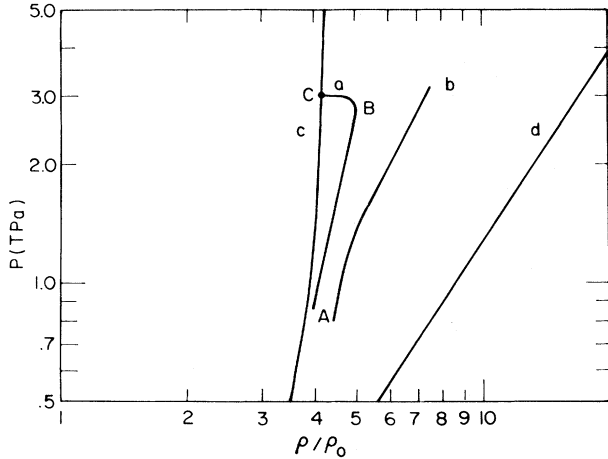


FIG. 5. Thermodynamic trajectories of the curve a, shock front zone and curve b, pile-up zone. Also shown are curves c, the Hugoniot and d, the adiabat.

Another proposal is¹⁸

$$P = 0.80 \left[\frac{I}{10^{14} \text{ W/cm}^2} \right]^{0.75} \text{ TPa} . \quad (3.3)$$

The values predicted by these equations are reasonably close to each other and our values in the shock front zone are in agreement with them,

$$P = 1.16 \left[\frac{I}{10^{14} \text{ W/cm}^2} \right]^{0.78} \text{ TPa} . \quad (3.4)$$

The higher coefficient in Eq. (3.4) results from the basic difference between the calculations: Equation (3.4) refers to the maximum pressure available in the plasma whereas Eqs. (3.2) and (3.3) describe the pressure at a constant depth of 25 μm (Ref. 2) and 10 μm ,¹⁸ where the pressure does not necessarily attain its maximum value. The agreement between our computations and Eqs. (3.1) and (3.2) can be regarded as an indication of the accuracy of our results.

Figure 5 describes the thermodynamic trajectories of the shock front and the pile-up zone in the P - ρ plane. The shock front, curve a, is generally quite close to the Hugoniot, curve c, but at early times (portion A-B) the two curves do not completely coincide. In fact, during this time period the shock front is accelerated into the cold material (see next section). Only at later times, $t \geq \tau_L$, does the shock front join the Hugoniot (portion B-C), when a final, constant velocity well-defined shock wave is formed.

The rear part, the pile-up zone, of the compression wave behaves quite differently. At early times it undergoes a rather constant acceleration. It follows a thermodynamic trajectory in a P - ρ plane which is somewhere between the Hugoniot and an

adiabat, curve b in Fig. 5, and can be described by a relation of the form

$$P = P_0 \left[\frac{\rho}{\rho_0} \right]^\alpha \quad (3.5)$$

with $\alpha = 2.0$ and $P_0 = 0.0575 \text{ TPa}$.

It is shown in the Appendix, that when a compression wave's motion has a constant acceleration, the rate of change of the pressure and the density are related by

$$\frac{dP}{dt} = (at + v_0)^2 \frac{d\rho}{dt} . \quad (3.6)$$

Substituting Eq. (3.5) into (3.6) one gets the time evolution of the pressure and density in the pile-up zone

$$\rho(t) = \rho(0) \left[1 + \frac{at}{v_0} \right]^{2/(\alpha-1)} , \quad (3.7)$$

$$P(t) = P(0) \left[1 + \frac{at}{v_0} \right]^{2\alpha/(\alpha-1)} , \quad (3.8)$$

where a is the acceleration $\rho(0)$, $P(0) = P_0 \rho(0) / \rho_0$, and $v_0^2 = P(0) / \rho(0)$ are the density, pressure, and the shock velocity extrapolated to $t = 0$.

Figure 6 shows the time history of $[\rho(t)/\rho_0]^{1/2}$ and $[P(t)/P_0]^{1/4}$. For $\alpha = 2$, Eqs. (3.7) and (3.8) predict that these two functions should be equal and rise linearly with time. These two features are satisfied with excellent accuracy (see Fig. 6).

The results listed here for aluminum hold qualitatively for polyethylene CH_2 as well. The two regions of the compression wave described above, pile-up zone and shock front zone, can be identified in the same way as for aluminum.

The values of the pressure, compression, and temperature in the pile up as well as shock front zones of a shock wave propagating in pure aluminum or polyethylene slabs are listed in Tables I and II, respectively.

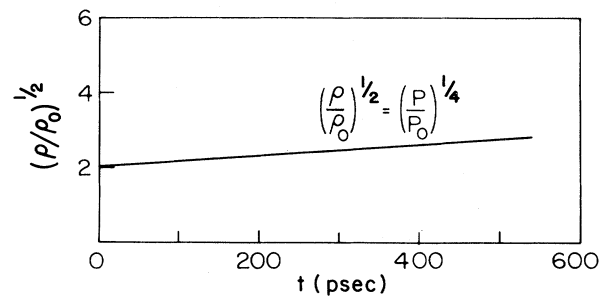


FIG. 6. Variation of $[\rho(t)/\rho_0]^{1/2}$ and $[P(t)/P_0]^{1/4}$ vs time for the case of Fig. 1. The two lines are indistinguishably close to each other.

TABLE I. Maximum pressure, compression, and the corresponding temperature at both the pile-up zone and shock front zone of a laser-driven compression wave in a planar aluminum slab. The following quantities are also listed: The time when the maximum values are attained as well as the depth of the shock front, the compression wave thickness, and the compressed mass at this instant.

Al	$I(\text{W}/\text{cm}^2)$ $\tau(\text{psec})$	3×10^{14}			3×10^{13}	
		300	600	1000	300	600
Pile-up zone						
Maximum pressure (TPa)		3.61	3.11	2.78		0.52
Maximum compression		7.2	7.5	7.7		6.2
temperature (10^5 K)		2.0	2.0	1.7		0.68
Time of occurrence						
of maximum values (psec)		300	540	810		550
Shock front zone						
Maximum pressure (TPa)		3.25	3.00	2.44		0.41
Maximum compression		4.6	5.0	5.0		4.0
temperature (10^5 K)		2.3	2.2	1.9		0.76
General						
Depth in the target (μm)		9.42	15.3	21.0		6.3
Compression wave thickness (μm)		1.78	2.89	4.04		1.17
Mass in compression wave at time						
of maximum pressure (mg/cm^2)		2.8	4.9	6.9		2.0

IV. SHOCK-WAVE VELOCITY IN PURE MATERIALS

Shock-wave velocity was calculated from code simulations separately for pure polyethylene and aluminum slabs, for laser intensities of 3×10^{13} – 3×10^{14} W/cm^2 and modified Gaussian pulse shapes with width of 300, 600, and 1000 psec. In this section we concentrate on the velocity of the shock-front zone, because this is an experimentally

measurable quantity.

Generally, three different phases can be distinguished during the time history of the shock-front velocity: (i) a phase of acceleration, (ii) a phase of constant velocity and finally, (iii) a phase of deceleration. Both the duration and the value of the acceleration and the velocity are dependent on the material and the laser beam intensity.

If the shock front would behave as a pure shock wave satisfying the Hugoniot relation, then, of

TABLE II. The same as Table I for a polyethylene slab.

CH ₂	$I(\text{W}/\text{cm}^2)$ $\tau(\text{psec})$	3×10^{14}			3×10^{13}	
		300	600	1000	300	600
Pile-up zone						
Maximum pressure (TPa)		3.68	3.58	3.21	0.55	0.53
Maximum compression		9.0	13.0	12.7	7.2	7.7
temperature (10^5 K)		1.28	1.04	1.24	0.39	0.35
Time of occurrence of						
maximum values (psec)		380	580	970	330	530
Shock front zone						
Maximum pressure (TPa)		3.70	2.71	2.22	0.50	0.50
Maximum compression		5.3	5.3	4.8	5.0	4.8
temperature (10^5 K)		1.80	1.51	1.40	0.47	0.48
General						
Depth in the target (μm)		21.1	28.5	42.8	5.0	9.9
Compression wave thickness (μm)		2.98	4.45	4.10	1.1	1.60
Mass in the compression wave at						
maximum pressure (mg/cm^2)		5.8	11.0	9.7	1.8	2.7

TABLE III. Accelerations and velocities of the shock front propagation in a polyethylene slab at various times of the laser irradiation. For $I=3 \times 10^{13}$ W/cm² the values given for $0 \leq t \leq 0.3\tau$ correspond to the whole time interval $0 \leq t < 0.8\tau$. $\overline{\Delta X}$ is the average deviation of the shock front position from the values predicted by the linear or quadratic forms (4.1) or (4.2).

	$I(\text{W/cm}^2)$ $\tau(\text{psec})$	3×10^{14}			3×10^{13}	
		300	600	1000	300	600
$0 \leq t < 0.3\tau$	a (10^{15} cm/sec ²)	27.0	19.7	10.6	3.0	2.0
	v_0 (10^6 cm/sec)	2.0	1.5	1.5	1.6	1.2
	$\overline{\Delta X}$ (10^{-4} cm)	0.05	0.06	0.2	0.05	0.06
$0.3\tau \leq t < 0.8\tau$	a (10^{15} cm/sec ²)	0	2.4	4.6	3.0	2.0
	v_0 (10^6 cm/sec)	6.0	4.4	2.4	1.6	1.2
	$\overline{\Delta X}$ (10^{-4} cm)	0.14	0.13	0.2	0.05	0.06
$0.8\tau \leq t \leq 2\tau$	v_0 (10^6 cm/sec)	6.6	5.7	5.5	2.76	2.5
	$\overline{\Delta X}$ (10^{-4} cm)	0.04	0.07	0.3	0.05	0.15

course, there would be no acceleration of the shock front. However, as we have seen in Sec. III, even the frontal portion of the compression wave is not a pure single-shock wave, therefore acceleration of the shock front is expected, as given by Eqs. (3.7) and (3.8).

Owing to the complexity of the driving-force structure even a constant-acceleration motion may seem an oversimplification of the problem, but it was found that the propagation of the shock wave can be divided into the periods described previously where constant acceleration or constant velocity can describe the shock-wave motion with sufficient accuracy.

The acceleration and the velocity were computed by fitting the shock front position $X(t)$ to linear or quadratic functions of time

$$X(t) = X_0 + v_0 t, \quad (4.1)$$

$$X(t) = X_0 + v_0 t + \frac{1}{2} a t^2, \quad (4.2)$$

for various time periods. The fit was accepted if a given set of constant parameters X_0 , v_0 , and a could describe the shock front position with an accuracy of better than $0.1 \mu\text{m}$. If the average accuracy using a quadratic form (4.2) was not much of an improvement relative to the linear form (4.1) we preferred the linear equation concluding that the shock propagation is a constant-velocity motion.

Regarding the shock velocity in CH₂, at a laser intensity of 3×10^{14} W/cm², three time periods can be distinguished within the time limits of our computations. First there is a rapid acceleration which lasts from $t=0$ until $t \approx 0.3\tau$, where τ is the laser pulse width (see Table III). Between $0.3\tau \leq t \leq 0.8\tau$ the acceleration continues at a decreased rate. The dis-

inction between this and the first time period reflects the fact that the acceleration is generally not constant. For $I=3 \times 10^{13}$ W/cm² in CH₂ targets and for all the aluminum targets the distinction between these two time periods was not so sharp as to warrant division into two different accelerations, so that for this intensity an average acceleration for the whole period $0 < t \leq 0.8\tau$ was used. Finally, a constant-velocity motion for $0.8\tau \leq t < 2\tau$ can be identified. This behavior of the shock front position $X(t)$ versus time is illustrated in Fig. 7 for the case of a CH₂ slab irradiated by an $I=3 \times 10^{14}$ -W/cm², $\tau=600$ -psec laser beam.

Tables III and IV show the values of the accelera-

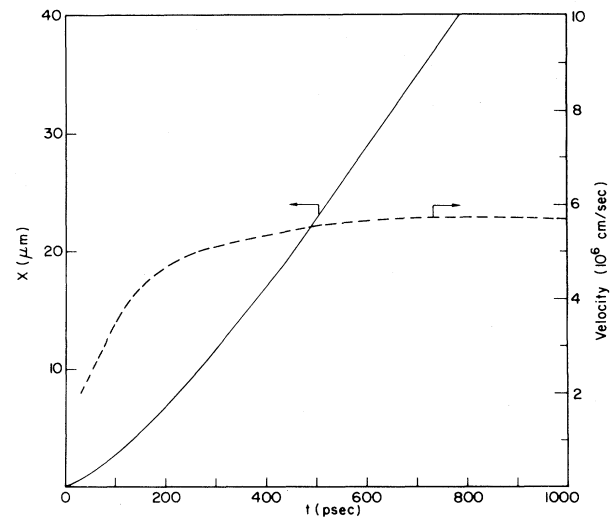


FIG. 7. Shock front position (—) and velocity (---) vs time in a CH₂ slab. The irradiation conditions are the same as in Fig. 1.

TABLE IV. Same as Table III for an aluminum slab.

	$I(\text{W/cm}^2)$ $\tau(\text{psec})$	3×10^{14}			3×10^{13}
		300	600	1000	600
$0 \leq t < 0.8\tau$	a (10^{15} cm/sec ²)	9.0	4.3	3.0	2.0
	v_0 (10^6 cm/sec)	1.8	1.7	1.5	0.6
	$\overline{\Delta X}$ (10^{-4} cm)	0.06	0.06	0.07	0.06
$0.8\tau \leq t < 2\tau$	v_0 (10^6 cm/sec)	4.1	3.8	3.3	1.6
	$\overline{\Delta X}$ (10^{-4} cm)	0.20	0.17	0.19	0.12

tion and the velocities of the shock waves at various laser intensities. Accelerations of the order of $(0.3-3) \times 10^{16}$ cm/sec² develop at the early stage of the laser pulse, and final velocities of the order of $(1-6) \times 10^6$ cm/sec are attained during the constant-velocity period.

The final velocity dependence on the peak intensity can be deduced in the following way: If the intensity is high enough so that the compression of the shock wave is close to its asymptotic value, then one can insert into the equation of the shock velocity [Eq. (A1) in the Appendix] $P_1 \gg P_0$, $V_0 - V_1 = \text{const}$, to find that

$$v_s \sim P_1^{1/2}, \quad (4.3)$$

using Eq. (3.2) this implies

$$v_s \sim I^{0.41}. \quad (4.4)$$

From the values of Table IV one finds

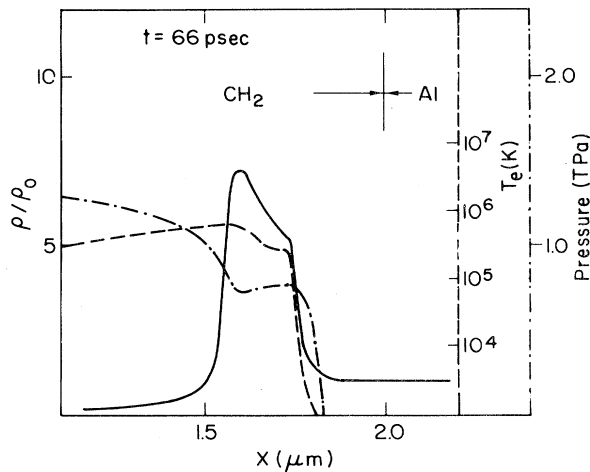


FIG. 8. Spatial distribution of compression (—), pressure (---), and temperature (-·-·-) in a compression wave driven into a 2- μm CH₂ on aluminum target irradiated by an $I = 2 \times 10^{14}$ -W/cm², $\tau = 300$ -psec laser beam at $t = 66$ psec after the beginning of the laser pulse.

$$\begin{aligned} v_s(I = 3 \times 10^{14} \text{ W/cm}^2, \tau = 600 \text{ psec}) \\ v_s(I = 3 \times 10^{13} \text{ W/cm}^2, \tau = 600 \text{ psec}) \\ = \frac{3.8 \times 10^6 \text{ cm/sec}}{1.6 \times 10^6 \text{ cm/sec}} = 2.38 \quad (4.5) \end{aligned}$$

in good agreement with the value of $10^{0.41} = 2.57$ predicted by Eq. (4.4). Reversing this procedure we find that Eq. (4.5) predicts a $v_s \sim I^{0.38}$ relationship, in reasonable agreement with both (3.2) and (3.3).

V. GENERAL BEHAVIOR OF SHOCK-WAVE PROPAGATION ACROSS THE INTERFACE BETWEEN TWO MATERIAL MEDIA

Two cases of shock-wave propagation in layered targets were studied which behave quite differently from each other (a) CH₂ on Al and (b) Al on CH₂. Of these, the first one turns out to be the more interesting.

A. Polyethylene on aluminum (CH₂ on Al)

Figures 8–13 show the evolution of the compression, pressure, and temperature in a target of a 2- μm

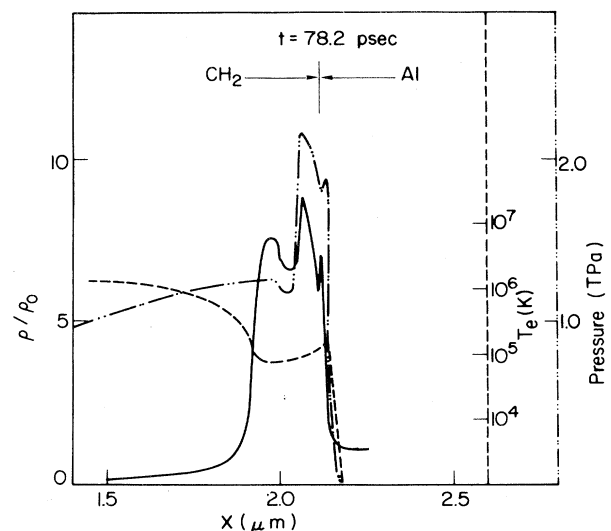
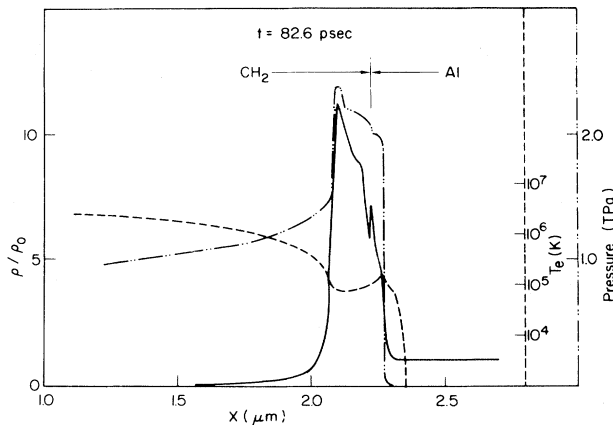
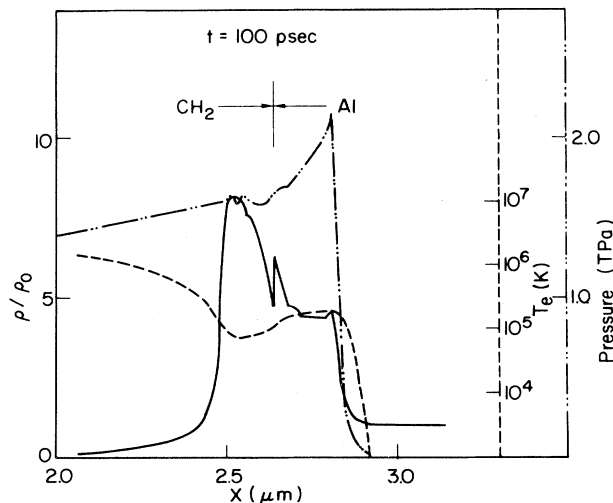
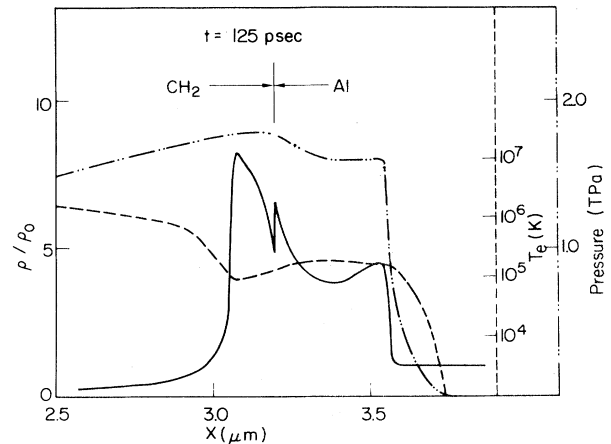


FIG. 9. Same as Fig. 8 at $t = 78.2$ psec.

FIG. 10. Same as Fig. 8 at $t = 82.6$ psec.

CH₂ layer mounted on a 2.5- μm aluminum slab irradiated by a 2×10^{14} -W/cm², 300-psec wide modified Gaussian pulse.

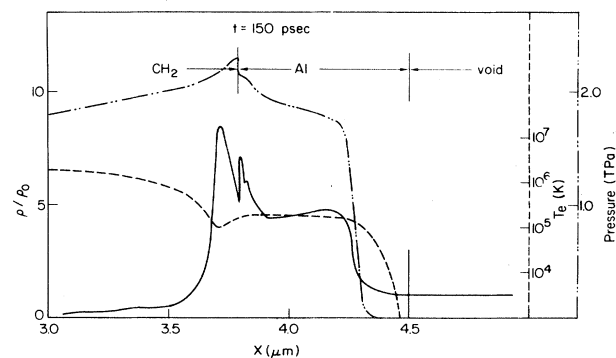
At early times, when the compression wave still propagates in the CH₂ layer, it has the properties that were already discussed in Sec. III (see Fig. 8). When the shock wave hits the interface between the two materials, it splits into two parts: A shock wave is transmitted into the aluminum support (see Fig. 9) and a second shock wave is reflected back into the polyethylene layer. As the impedance of aluminum is higher than that of polyethylene, this backreflected wave is also a shock wave.¹¹ The backreflected wave moves into a heated and compressed material increasing the compression and the pressure even more. A similar mechanism of backreflection is used in shock tubes to increase the pressure and compression of gases.¹¹ Finally, when the backreflected shock front collides with the pile-up zone of the incoming wave, a compression of $\rho/\rho_0 = 11.4$

FIG. 11. Same as Fig. 8 at $t = 100$ psec.FIG. 12. Same as Fig. 8 at $t = 125$ psec.

and a pressure of $P = 2.4$ TPa are achieved (see Fig. 10), as compared to values of $\rho/\rho_0 = 7.2$ and $P = 1.12$ TPa in a pure polyethylene target (see Fig. 8). It is shown below that by properly choosing the thickness of the CH₂ layer even higher compressions and pressures can be attained without changing the laser intensity or energy. These high compressions and pressures exist for a rather long time (see Figs. 11 and 12) pushing a strong shock wave into the aluminum layer. In the example given here, the laser intensity goes on increasing until $t = 300$ psec, leading to a further pressure increase (see Fig. 13) but this time the increase originates from the growth of the laser intensity.

B. Aluminum on polyethylene (Al on CH₂)

The case of a target composed of a 1- μm aluminum slab mounted on a 17- μm CH₂ support is shown in Figs. 14–17, under the same laser irradiation conditions as the previous case. None of the features mentioned above, are seen here. The basic difference between the two configurations is the fact that in the Al on CH₂ case the wave reflected back

FIG. 13. Same as Fig. 8 at $t = 150$ psec.

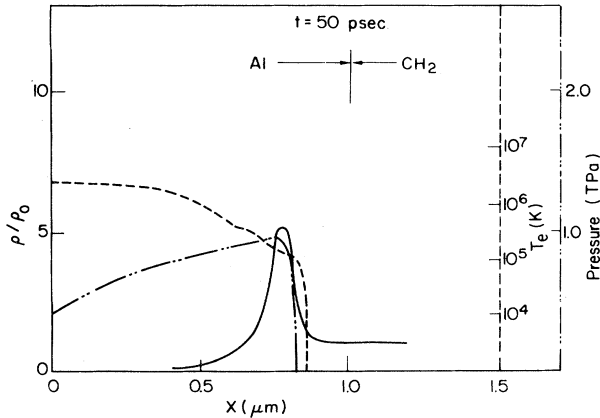


FIG. 14. Spatial distribution of compression (—), pressure (---), and temperature (-·-·-) in a compression wave driven into a 1- μm aluminum on polyethylene target irradiated by an $I=2 \times 10^{14}$ -W/cm², $\tau=300$ -psec laser beam at $t=50$ psec after the beginning of the laser pulse.

into the aluminum layer is a rarefaction wave which reduces the pressure on the interface (see Figs. 15 and 16) in contrast to the backreflected shock wave in the CH₂ on Al case. For the sake of completeness, the rarefaction wave produced on “unloading,” i.e., punch-through, is also shown in Fig. 17. As this Al on CH₂ case does not show any interesting physical features in the following we shall concentrate only on the CH₂ on Al configuration.

VI. PRESSURE, COMPRESSION, AND TEMPERATURE IN THE CH₂ ON Al CONFIGURATION

In Sec. III we found that the pressure and compression attain their maximum values at $t \approx \tau$ (τ —laser pulse rise time). If the backreflection of

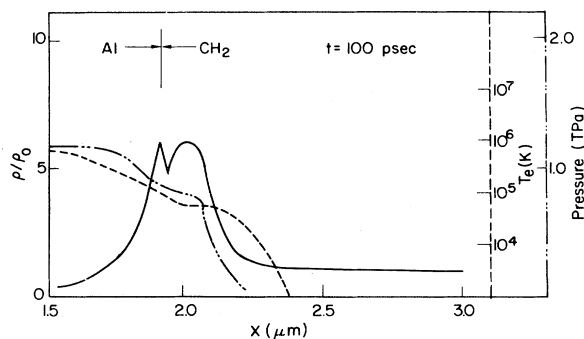


FIG. 15. Same as Fig. 14 at $t=100$ psec.

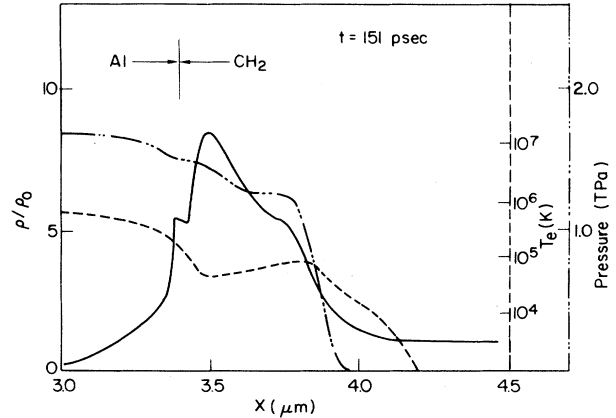


FIG. 16. Same as Fig. 14 at $t=151$ psec.

the compression wave from the CH₂-Al interface occurs at the same time, then one would expect that the pressure and compression would achieve their maximum possible value at this time for a given laser intensity and energy. This condition imposes requirements on the CH₂ layer thickness: To obtain the highest possible pressure and compression on the interface, the CH₂ layer thickness must be adjusted so that the compression wave will arrive at the interface at $t \approx \tau$.

This behavior is shown in Table V and Figs. 18 and 19. Data of the maximum pressure and compression on the interface as well as the temperature on the interface at the instant of maximum pressure are given in Table V for $I=3 \times 10^{14}$ W/cm² and pulse rise times of 300, 600, and 1000 psec. A less complete set of computational results

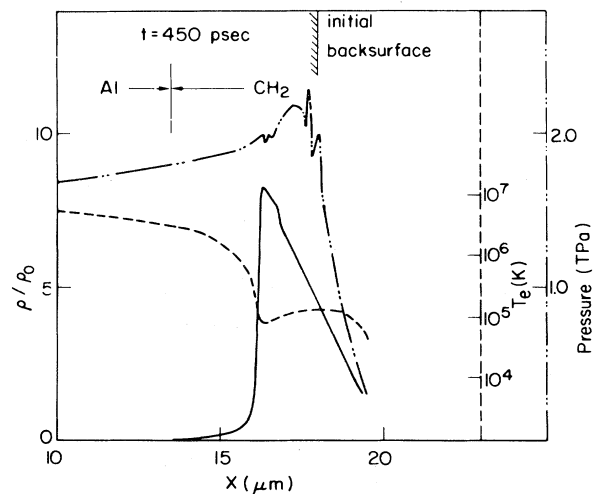


FIG. 17. Same as Fig. 14 at $t=450$ psec, i.e., after the punch-through of the backsurface by the shock wave. The abscissa scale is reduced by a factor of 10 relative to Figs. 14–16.

TABLE V. Maximum pressure and compression developed on the interface of CH₂-Al-layered targets for various laser intensities, pulse rise times, and CH₂-layer thicknesses. Persistence time of the transient high pressure, the shock-wave transit time in the CH₂ layer, and the temperature developed on the interface are also listed.

CH ₂ -layer thickness (μm)	Laser intensity (W/cm ²)	Pulse rise time (psec)	Maximum pressure on interface (TPa)	Maximum compression on interface	Temperature on interface (10 ⁵ K)	Decay time of high pressure (psec)	Time of arrival of shock at interface (psec)
5	3×10 ¹⁴	300	51	11.9	2.0	40	126
15	3×10 ¹⁴	300	75	16.5	3.4	110	298
25	3×10 ¹⁴	300	54	12.3	3.4	250	442
5	3×10 ¹⁴	600	33	12.1	1.5	70	157
9	3×10 ¹⁴	600	45	13.2	1.8	90	251
15	3×10 ¹⁴	600	55	16.8	2.1	120	365
20	3×10 ¹⁴	600	64	18.7	2.4	150	459
25	3×10 ¹⁴	600	68	19.5	2.7	180	539
30	3×10 ¹⁴	600	65	19.2	3.1	200	625
40	3×10 ¹⁴	600	63	15.9	2.4	200	782
20	3×10 ¹⁴	1000	45	14.8	1.8	190	541
40	3×10 ¹⁴	1000	54	19.3	2.1	370	916
2	2×10 ¹⁴	300	23	11.3	1.4	40	72
7.5	2×10 ¹⁴	300	44	13.5	1.9	150	200
15	3×10 ¹³	300	7.1	9.4	0.68	130	664
25	3×10 ¹³	600	8.3	8.3	0.84	240	1153

for intensities of $I=2\times 10^{14}$ and 3×10^{13} W/cm² are also shown. The data for the pressure and compression show a clear maximum for these quantities at the appropriate CH₂ layer thickness (Figs. 18 and 19). It is apparent from Table V (last column) that the maximum values are attained when the compression wave is backreflected from the interface at $t\approx\tau$. For $I=3\times 10^{14}$ W/cm², this corresponds to a CH₂ thickness of ~ 15 μm for $\tau=300$ psec ~ 25 μm for $\tau=600$ psec, and ~ 40 μm for $\tau=1000$ psec.

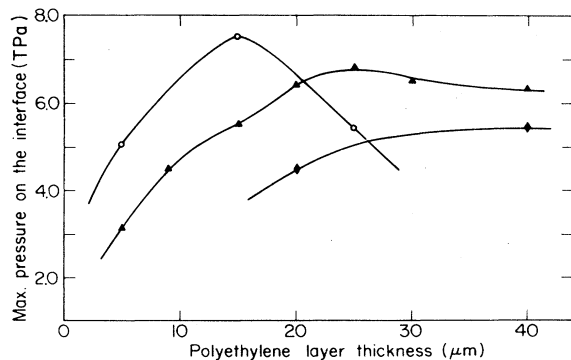


FIG. 18. Pressure developed on the CH₂-Al interface vs the CH₂-layer thickness. Lines which connect the points of a given laser intensity and pulse width do not describe any particular function, but are inserted as a visual aid only. ○, $I=3\times 10^{14}$ W/cm², $\tau=300$ psec; ▲, $I=3\times 10^{14}$ W/cm², $\tau=600$ psec; ◆, $I=3\times 10^{14}$ W/cm², $\tau=1000$ psec.

For the optimum CH₂ thickness a compression of $\rho/\rho_0=19.5$ is obtained as compared to $\rho/\rho_0=13.0$ for the single layer case, and pressures of 7.5, 6.6, and 5.4 TPa for the three rise times as compared to 3.7, 3.6, and 3.2 TPa for the corresponding single layer case. To emphasize this point we recall that this increase of a factor of 1.5 in the compression and a factor of 2 in the pressure originates from the impedance mismatch between the two materials.

Of special importance is the length of time the high pressure and compression remain on the interface. In fact, if the decay time of the pressure were very short relative to the plasma characteristic times, this effect would have no measurable influence on the shock-wave parameters. However, as can be seen from Table V, column 7, these high

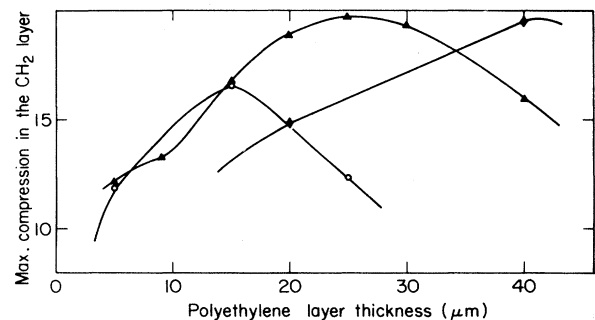


FIG. 19. Same as Fig. 18 for the compression on the interface.

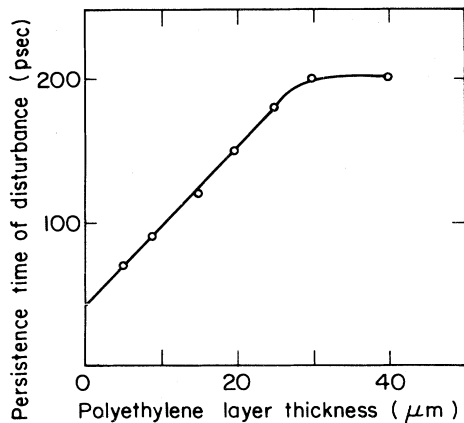


FIG. 20. Persistence time of the high pressure on the CH_2 -Al interface vs the CH_2 -layer thickness.

values are effective for rather long times, up to 50% (or perhaps even more) of the laser pulse rise time. The persistence time of the high pressure is an almost linearly rising function of the CH_2 layer thickness (see Fig. 20) reflecting the fact that the compression wave broadens almost linearly with the time of propagation into the target. For the thicker CH_2 layers this persistence time is long enough to have appreciable influence on the shock-wave velocity in the plasma.

The rather long decay time compared to the shock transit time of the transient high pressure on the interface is a basic difference between laser-driven and explosion-generated shock waves. The much smaller dimensions of the targets used in the laser-plasma

experiments and the much shorter time scales enhance the effects of these transients, which generally do not have any influence on the larger dimension explosion-generated shock-wave experiments.

VII. SHOCK VELOCITY IN A CH_2 ON AL LAYERED TARGET

The development of very high transient pressures on the interface greatly alters the propagation of the shock front into the aluminum support. Figure 21 shows the shock-front position versus time for a target of a 25- μm polyethylene layer on an aluminum support irradiated with an $I = 3 \times 10^{14} \text{ W/cm}^2$, $\tau = 600$ -psec laser beam. For comparison, the positions of the critical surface, the ablation surface, the CH_2 -Al interface, and the pile-up zone positions are shown as well. (The left-hand side scale in Fig. 21, relevant to the critical surface position, is reduced by a factor of 10 relative to the scale on the right-hand side.) The corresponding velocities of the shock front, the pile-up zone, and the interface are shown in Fig. 22. These figures reveal the special behavior of shock-wave propagation in a layered target. The propagation of the shock wave in the polyethylene layer has already been described in Sec. III. When the shock front crosses the interface between the two layers at about $t = 540$ psec, large disturbances of the simple wave motion seem to occur. In particular, the shock is accelerated in two separate periods (see Fig. 22) for about 150 psec after the crossing and only later is a constant velocity

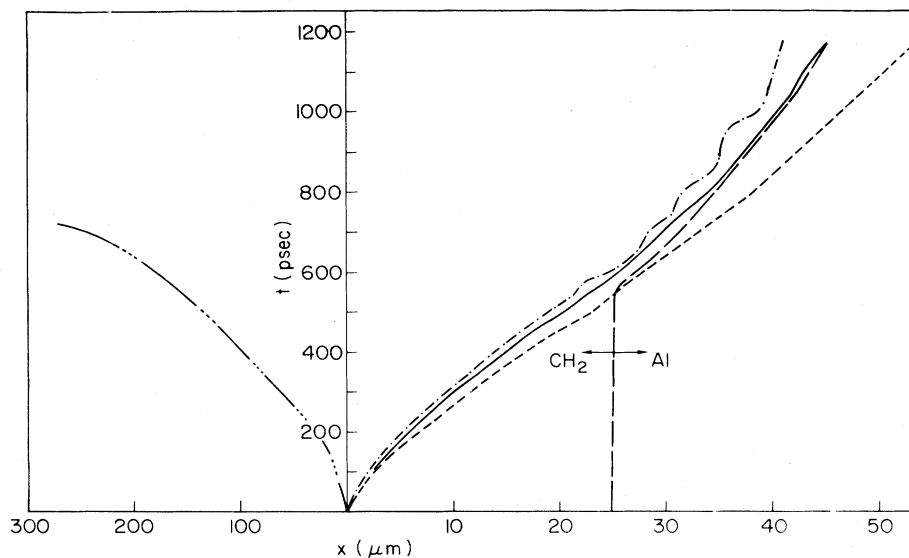


FIG. 21. Positions of the critical surface (---), the ablation surface (-·-·-·), the pile-up zone (—), the CH_2 -Al interface (—), and the shock front (---) vs time. The target is a 25- μm CH_2 layer on an aluminum support. Laser intensity is $3 \times 10^{14} \text{ W/cm}^2$ and its pulse rise time is 600 psec.

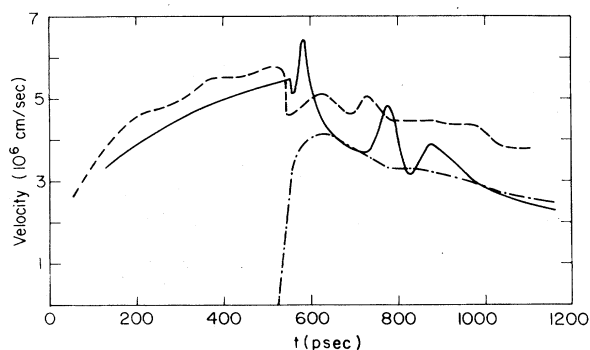


FIG. 22. Velocities of the shock front (---), the CH₂-Al interface (- · - · -), and the pile-up zone (—) vs time, as derived from Fig. 20.

ty motion attained. During the time the acceleration takes place, the increase of the shock front velocity is about 10%.

Much more complicated is the pile-up zone motion, which is strongly affected by the backreflection of shock waves from the interface. For the velocity of this portion of the compression wave, fluctuations of up to 20% occur at rather irregular intervals for as long as 400 psec after the shock arrival at the interface (see Fig. 22). These fluctuations indicate the rather complex nature of the interference of the shock waves propagating into the material with those reflected back from the interface.

The average acceleration of the shock front in the aluminum support and the duration of this acceleration time are listed in Table VI, for a laser intensity of 3×10^{14} W/cm², pulse rise times of 600 psec, and various CH₂ layer thicknesses. Table VI shows that the acceleration time is closely related to the persistence time of the high pressure on the interface, which was discussed in the previous section (see Table V). In fact, within the limits of the accuracy of our computations, these two times can be considered identical indicating the close relationship between the transient high pressure on the interface

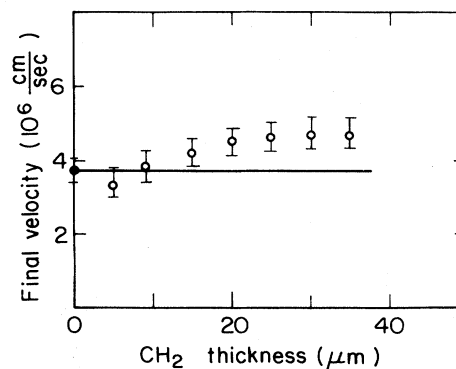


FIG. 23. Final velocity of the shock front in the aluminum support of CH₂-Al targets irradiated by an $I = 3 \times 10^{14}$ W/cm², $\tau = 600$ -psec laser beam. Horizontal line shows the corresponding velocity in a pure aluminum slab target.

and the acceleration of the shock front into the aluminum support.

The acceleration of the shock front is rather high for the 5- μ m CH₂-layer case, but it stabilizes around a constant value of about 7.7×10^{15} cm/sec² for targets with a 9- to 25- μ m polyethylene layer facing the laser beam. For thicker layers the acceleration of the shock front into the aluminum support decreases due to the lower pressures developing on the interface.

The final constant velocity of the shock front is also given in Table VI, and plotted versus the CH₂ layer thickness in Fig. 23. This velocity seems to be an increasing function of the CH₂-layer thickness, which for very thick layers attains an asymptotic value of about 4.7×10^6 cm/sec. This asymptote is a result of the lower value of the acceleration and the longer acceleration time in the thicker layer targets. However, the most interesting fact about the final constant velocity in the CH₂-Al target is the point, that for every CH₂ thickness (including probably the 5- μ m case as well) the final shock front velocity in the aluminum support in a layered target is higher than the corresponding value of 3.8×10^6

TABLE VI. Acceleration and the final constant velocity of the shock front in the aluminum support of CH₂-Al-layered targets. Laser intensity is 3×10^{14} W/cm² and the pulse rise time is 600 psec. $\Delta\bar{X}$ is the average deviation of the fitted value of the shock front position from the computed values. Time duration of the acceleration is also listed.

	CH ₂ -layer thickness (μ m)	5	9	15	20	25	30	40
Period of shock front acceleration	Acceleration (10^{15} cm/sec ²)	16.0	7.8	8.2	7.5	7.7	4.2	2.4
	Initial velocity (10^6 cm/sec ²)	0.6	1.9	1.2	1.0	3.1	2.1	2.8
	$\Delta\bar{X}$ (μ m)	0.03	0.03	0.03	0.03	0.01	0.02	0.02
	Duration (psec)	70	90	100	110	130	150	200
Period of constant-velocity propagation	Average velocity (10^6 cm/sec)	3.4	3.8	4.1	4.5	4.6	4.7	4.7
	$\Delta\bar{X}$ (μ m)	0.17	0.07	0.22	0.22	0.21	0.24	0.34

cm/sec in a pure aluminum slab target (see Table IV). This can be understood in terms of the higher (ablation) pressure in CH₂ (the lighter material) than in Al. Therefore, the final pressure in the Al substrate of the CH₂-Al target and hence the shock velocity, is higher than in an all Al target.

VIII. DISCUSSION

In this paper we have concentrated on the complex nature of a laser-driven compression wave. It was shown that the compression wave can be divided into two portions which smoothly join each other. The pile-up zone in the rear of the compression wave has a higher compression and lower temperature than the shock front region. This pile-up zone follows a thermodynamic trajectory which is closer to the adiabat than the shock front whose trajectory is close to, but not completely coincident with, the corresponding Hugoniot curve. These conclusions hold for both aluminum and polyethylene targets.

The time history of the compression wave is also rather complex. At early times it behaves as a multiple-shock wave. During this period the compression wave front undergoes an acceleration. Eventually this multiple-shock wave coalesces into a single-shock wave which stabilizes on the Hugoniot curve. When this phase is approached, the wave attains a constant velocity of propagation into the cold material.

Particular attention was paid to the problem of the shock front motion, as this can be measured to an accuracy which is necessary for EOS measurements. We found that a constant velocity motion is achieved only for $t \geq 0.8\tau$. At earlier times the shock front is accelerated. This point must be carefully taken into account when planning experiments of this type.

We have also studied the propagation properties of a laser-driven shock wave across the interface of a polyethylene-aluminum layered target. The combination of these two materials seems to be a good illustration of the behavior of the shock wave when it crosses the interface of two materials with a significant impedance mismatch.

For the propagation properties of a shock wave across the interface we have found the following.

(a) A backreflected shock wave is generated on the interface of a CH₂-Al target, in contrast to a backreflected rarefaction wave when the materials are in the reverse order.

(b) When the backreflected shock wave in a CH₂-Al target collides with the rear portion, the pile-up zone, of the incoming wave, a region of high pressure and compression develops around the interface.

(c) The persistence time of the high pressure on

the interface is not short relative to the characteristic times of the plasma, so that it has appreciable influence on the shock-wave propagation into the aluminum support.

(d) The pressure and compression on the interface are optimizable by adjusting the CH₂-layer thickness. The optimum occurs when the shock front transit time in the CH₂ layer approximately equals the laser pulse rise time. In the case study of this paper an increase of 50% in the compression and a factor of 2 increase in the pressure are obtained.

(e) During the persistence of the transient high pressure on the interface, the shock front is accelerated into the aluminum support in a rather complex manner. The final shock velocity in such a composite target is always higher than in a single layer target under the same laser irradiation conditions.

A few words on the validity and the accuracy of our results are in order. In Sec. III we have shown that our calculations are reasonably close to others' computational results. Nevertheless, slight quantitative modifications to our results are possible by incorporating more features into our hydrodynamic code, such as fast electron preheat, more accurate equation-of-state, parametric instabilities, and anomalous energy transport. As most of these processes are effective only at much higher laser intensities than the ones used in this paper, their inclusion will cause only minor quantitative changes in our results. However, our general conclusions will not be influenced by any of the above processes so that the qualitative consequences of the behavior of the compression wave and the scaling laws of its parameters would remain valid.

APPENDIX: PRESSURE-DENSITY RELATION FOR CONSTANT-ACCELERATION SHOCK PROPAGATION

Shock-wave velocity can be found from the slope of the straight line connecting the states before and behind a shock wave, on a Hugoniot curve,¹¹

$$v_{s,i-1}^2 = V_{i-1}^2 \frac{P_i - P_{i-1}}{V_{i-1} - V_i} \quad (\text{A1})$$

If the discontinuity originates from the coalescence of many weak shock waves, then the thermodynamic trajectory of this discontinuity is a series of jumps from one Hugoniot curve to another and the instantaneous shock velocity is found from (A1),

$$v_s^2(t) = V^2(t - \Delta t) \frac{P(t) - P(t - \Delta t)}{V(t - \Delta t) - V(t)} \quad (\text{A2})$$

If the transition between the Hugoniot curves is continuous we can assume $\Delta t \rightarrow 0$ and Eq. (A2) is

modified to

$$v_s^2(t) = -V^2(t) \frac{\dot{P}(t)}{\dot{V}(t)} = \frac{\dot{p}(t)}{\dot{\rho}(t)}, \quad (\text{A3})$$

where the dots denote time derivatives of the pressure, specific volume, and density. Assume that a constant-acceleration motion of the discontinuity develops with an acceleration a , then

$$a = \dot{v}_s(t) = \frac{d}{dt} \left[\frac{\dot{P}(t)}{\dot{\rho}(t)} \right]^{1/2} \quad (\text{A4})$$

whose solution is

$$\frac{\dot{P}(t)}{\dot{\rho}(t)} = (at + v_0)^2. \quad (\text{A5})$$

Assuming a thermodynamic relation $P = P(\rho(t))$, the time derivatives satisfy $\dot{P} = (\partial P / \partial \rho) \dot{\rho}$, and (A5) yields

$$\frac{\partial P[\rho(t)]}{\partial \rho} = (at + v_0)^2 \quad (\text{A6})$$

which gives the time evolution of a multiple-shock wave having constant acceleration.

The initial velocity v_0 is calculated from the initial conditions by

$$v_0^2 = \frac{\partial P(t=0)}{\partial \rho}. \quad (\text{A7})$$

- ¹R. J. Trainor, H. C. Graboske, K. S. Long, and J. W. Shaner, University of California Report No. UCRL-52562 (unpublished).
- ²R. M. More, in *Laser Interaction and Related Plasma Phenomena*, edited by H. J. Schwarz, H. Hora, M. J. Lubin, and B. Yaakobi (Plenum, New York and London, 1981), Vol. 5, p. 253.
- ³C. G. M. van Kessel and R. Sigel, *Phys. Rev. Lett.* **33**, 1020 (1974).
- ⁴C. G. M. van Kessel, *Z. Naturforsch.* **30a**, 1581 (1975).
- ⁵L. R. Veerer, J. C. Solem, and A. J. Lieber, *Appl. Phys. Lett.* **35**, 761 (1979).
- ⁶L. R. Veerer and J. C. Solem, *Phys. Rev. Lett.* **40**, 1391 (1978).
- ⁷R. J. Trainor, J. W. Shaner, J. M. Auerbach, and N. C. Holmes, *Phys. Rev. Lett.* **42**, 1154 (1979).
- ⁸R. P. Goldstone, R. F. Benjamin, and R. B. Schultz, *Appl. Phys. Lett.* **38**, 223 (1981).
- ⁹D. Billon, D. Cognard, J. Launspach, C. Patou, D. Redon, and D. Schirmann, *Opt. Commun.* **15**, 108

(1975).

- ¹⁰C. E. Ragan III, *Phys. Rev. A* **21**, 458 (1980).
- ¹¹Ya. B. Zeldovitch and Yu. P. Raiser, *Physics of Shock Waves and High Temperature Hydrodynamic Phenomena* (Academic, New York, 1966).
- ¹²S. Eliezer, L. Gitter, A. D. Krumbein, and D. Salzmann, *Phys. Lett.* **86A**, 464 (1981).
- ¹³A. Zigler, H. Zmora, and J. L. Schwob, *Phys. Lett.* **63**, 275 (1977).
- ¹⁴W. L. Wiese, M. W. Smith, and B. M. Miles, National Standards Reference Data Series, NSRDS-NBS 22, 1969 (unpublished).
- ¹⁵E. B. Goldman, Laboratory for Laser Energetics, University of Rochester Report No. 16 (unpublished).
- ¹⁶D. D. Clayton, *Principles of Stellar Evolution and Nucleosynthesis* (McGraw-Hill, New York, 1968), Table 2.3, p. 95.
- ¹⁷R. E. Kidder, *Nucl. Fusion* **8**, 3 (1968).
- ¹⁸P. C. Thompson, P. D. Roberts, N. J. Freeman, and P. T. G. Flynn, *J. Phys. D* **14**, 1215 (1981).